Supplementary Information (SI) for Journal of Materials Chemistry C.

Supplementary Information

Reducing the cell-to-module performance gap of inorganic perovskite by anisotropically-structured hole transport materials

Jin Wang,†[a] Xuran Wang,†[b] Peng Xu,[a] Xiangnan Sun,[a] Mingwei An,[b],* Wei Zhang,[a],* Yang Wang,[b] and Xiaoming Zhao[a],*

[a] State Key Laboratory of Mechanics and Control of Mechanical Structures, Key Laboratory for Intelligent Nano Materials and Devices of the Ministry of Education, Institute for Frontier Science, Nanjing University of Aeronautics and Astronautics, Nanjing 210016, China

[b] Strait Institute of Flexible Electronics (SIFE, Future Technologies), Fujian Normal University, Strait Laboratory of Flexible Electronics (SLoFE), Fuzhou, Fujian 350117, China

†These authors contributed equally to this work.

*Corresponding contributor. E-mail: ifemwan@fjnu.edu.cn (M. An), wei.zhang@nuaa.edu.cn (W. Zhang), xiaoming.zhao@nuaa.edu.cn (X. Zhao).

1. Experimental Section

1.1 Materials

PbI_2 (99.99%) was purchased from TCI America. CsI (99.5%), DMAI (99%), Spiro-OMeTAD (99%), Acetylacetone (> 99%) and titanium diisopropoxide (75 wt.% in isopropanol) were purchased from Sigma Aldrich. Chlorobenzene (> 99.8%) and Dimethylformamide (DMF) (99.8%) were purchased from Acros Organics. Bis(trifluoromethane)sulfonimide lithium salt (Li-TFSI) (99.95%) and FK-209 (99.95%) was purchased from Yingkou Advanced Election Technology Co., Ltd. Acetone, isopropanol and other solvents were purchased from Fisher Scientific. All chemicals were used as-received without further purification. Solar cell substrates are pre-patterned fluorine-doped tin-oxide-coated (FTO) glass obtained from Yingkou Advanced Election Technology Co., Ltd. SF-MPA-MCz was syntheized and purifed following the reported method.[1]

1.2 Device fabrication

Pre-patterned FTO substrates were cleaned with deionized water, acetone, isopropanol, and UV-Ozone cleaner. For the electron transport layer, a compact titanium dioxide (TiO_2) layer of about 40 nm was deposited by spray pyrolysis of 7 mL 2-propanol solution containing 0.6 mL titanium diisopropoxide bis(acetylacetonate) solution and 0.4 mL acetylacetone at 450 °C using oxygen as the carrier gas. The substrates were then treated by UV-Ozone for 15 minutes. SRL modification was conducted following our previous report.[2] After that, the substrates were rinsed in isopropanol and then dried under a flow of N_2. To prepare the $CsPbI_3$ active layer, a 0.6 M $CsPbI_3$ precursor solution was prepared by dissolving stoichiometric CsI, PbI_2, DMAI with 1:1:1.3 molar ratio in DMF. The precursor solution was cast on the substrate and then spun at 2800 rpm for 30 s. Then the films were thermally annealed at 215 °C for 4.5 minutes. All annealing processes were carried out in a dry box with controlled humidity of 23-25% R.H.

Subsequently, a hole transport layer was deposited on top of the active layer by spin-coating a Spiro-OMeTAD or SF-MPA-MCz solution at 3000 rpm for 30 s. To prepare Spiro-OMeTAD solution, 80 mg of Spiro-OMeTAD, 28.8 μL of *t*-BP, 17.5 μL of Li-TFSI (520 mg/mL in ACN), and 17.5 μL of FK-209 (300 mg/mL in ACN) were added into 1 ml of CB. SF-MPA-MCz solution in CB (28 mg/mL) was mixed with 12 μL of *t*-BP, 8 μL of Li-TFSI solution (520 mg/mL in ACN), and 8 μL of FK-209 (300 mg/mL in ACN). Finally, the solar cells were completed by thermal evaporation of 100-nm thick gold top electrodes. The active area (0.16 cm^2) was defined using a shadow mask. 100-nm and 200-nm MgF_2 layers were respectively evaporated onto the glass side of FTO substrates and the gold side of the devices as an anti-reflection layer and the initial protection layer.

1.3 Module fabrication

The modules connected in series were obtained by interconnecting P1, P2, and P3 through laser structuring using a laser scribing system equipped with a 1,064 nm laser with a maximum power of 20 W. The first laser scribing line (P1 line) was performed directly on the clean FTO substrates using a laser power of 10 W, a pulse width of 100 ns, and a repetition rate of 100 kHz, resulting in a scribe width of approximately 50 μm, which ensures complete electrical isolation of the bottom electrodes. The substrates were cleaned by sequentially washing with detergent, acetone and IPA, each step for 15 min and dried by nitrogen gas. Before use, the FTO was treated with UV ozone for 30 min. TiO_2 and SRL layers were deposited using the same method to single cells. $CsPbI_3$ precursor solution was blade-coated onto the substrates with a gap of 200 μm at a movement speed of 30 mm s^{-1}. A nitrogen knife operated at 25 psi was used during blade coating. After that, the wet films were annealed at 215 °C for 4.5 minutes. Afterwards, HTM solutions were blade-coated at a speed of 15 mm s^{-1} with a gap of 200 μm. After deposition of the functional layers, the second laser scribing line (P2 line) was laser-scribed with a reduced power of 6 W, a pulse width of 100 ns, and a repetition rate of 70 kHz, yielding a scribe width of about 150 μm. This step selectively removes the HTM and perovskite layers to expose the underlying FTO, creating interconnection windows for subsequent series connection. Then top contact comprising Au (100 nm) was deposited as electrode. Finally, the third laser scribing line (P3 line) was laser-scribed on the Au electrode using identical laser parameters (6 W, 100 ns, 70 kHz), resulting in a scribe width of approximately 100 μm, which electrically isolates adjacent sub-cells by cutting through the Au electrode and underlying layers down to the insulating P1 region. 100-nm and 200-nm MgF_2 layers were respectively evaporated onto the glass side of FTO substrates and the gold side of the devices as an anti-reflection layer and the initial protection layer. The geometric fill factor was around 0.93.

1.4 Characterization

XPS measurements were performed with a ThermoFisher Ultraviolet + X-ray Photoelectron Spectrometer using a monochromatic Al Kα X-ray of 24.8 W power. TRPL spectra were measured with an Edinburgh Instruments FLS1000 photoluminescence spectrometer. UPS measurements were performed with a Thermo Fisher Scientific ESCALAB XI+. The SEM images were obtained using a FEI Helios scanning electron microscope. AFM measurements were performed using a scanning probe microscope (Shimadzu SPM-9700HT). UV-vis absorption spectra were obtained on an Agilent Technologies Cary 5000 spectrophotometer. Ion migration activation energies were measured and extracted following reported methods.[3-5] We used lateral devices with structures of Au/perovskite/Au with channel length of 100 μm for these measurements. The conductivity of these devices was measured by applying a 20 V bias, corresponding to an average electrical field of 0.2 V μm^{-1}, under 10^{-6} Torr vacuum on a Lake Shore tabletop cryogenic probe station with a Keithley 4200-SCS semiconductor parameter analyzer. Sample temperature was controlled in a close-circle cryostat from 150 to 350 K. We first cooled the device to 150 K and waited an hour for the temperature to stabilize.

Subsequently, the device was heated to and stabilized at each temperature for 10 min before current measurements were performed. To avoid transient current spikes, which occurred in the first few seconds after bias, the conductivity was extracted from the device current at 120 s after the bias was applied. The *J-V* characteristics of solar cells were obtained using a Keithley 2400 source meter under simulated 1-sun AM 1.5G illumination (100 mW cm^{-2}) with a solar simulator (Enlitech, SS-F5-3A) and the light intensity was calibrated by a Si photodiode. The *J-V* measurements were carried out in ambient air. The devices were measured both in reverse scan (from 1.5 to -0.2 V, step 0.01 V) and forward scan (from -0.2 V to 1.5 V, step 0.01 V). The EQE was measured using an Enlitech EQE measurement system (QE-R3018).

1.5 Encapsulation and stability measurements

Before encapsulation, 200-nm MgF_2 was deposited on the Au side as the initial protection layer. Afterwards, the devices were encapsulated in a nitrogen glovebox. Single cells and modules were encapsulated by a combination of edge-sealing (UV-curable epoxy, EpoTech, OG159-2) and blanket-sealing (polyolefin encapsulant, Mitsui Solar TR02BA).[6] Operational stability studies were conducted according to the ISOS-L-3 protocol.[7] The light source was provided by metal-halide lamps with 100 mW cm^{-2} intensity. The current density versus voltage (*J-V*) characteristics were measured every hour. The initial values at the maximum power point (MPP) were obtained from each *J-V* sweep, and then the devices were kept at the MPP during operation by an active load system. To measure the damp-heat test of the encapsulated devices, we kept the solar cells at constant temperature and humidity (85 °C and 85% R.H.) in a testing chamber. The encapsulated devices were measured periodically after cooling of devices. For shelf stability studies, the unencapsulated devices were put in a testing chamber with controlled humidity of 25% R.H. and temperature of 40 °C.

1.6 DFT calculations

In this work, we utilized the CP2K software package to conduct ab initio molecular dynamics (AIMD) simulations. CP2K is a robust tool for quantum chemistry and solid-state physics modeling, particularly advantageous for large-scale systems. The software adeptly performs density functional theory (DFT) calculations and accommodates various computational methodologies, including a mixed Gaussian and plane-wave basis set. We set the plane-wave cutoff energy at 500 eV and employed the DZVP Gaussian basis set for all elements to ensure precise electronic structure characterization. Furthermore, we applied the Perdew-Burke-Ernzerhof (PBE) generalized gradient approximation (GGA) for the treatment of exchange-correlation effects, while dispersion interactions were corrected using the D3(BJ) method. This methodological framework enabled us to achieve results of high accuracy within reasonable computational limits. The corresponding input files are constructed with the assistance of multiwfn. Calculations identify the $CsPbI_3$ (001) plane as the most stable surface. To reduce computational costs, a 5×5×3 $CsPbI_3$ perovskite supercell was constructed. The electron wave functions were expanded using a plane-wave basis set with a kinetic energy cutoff of 400 eV. For K-point sampling, a 1×1×1 Monkhorst-Pack grid was applied in the irreducible Brillouin zone. A 40 Å vacuum region was added to the outer PbI_2 surface to avoid spurious interactions. A similar treatment was performed on the exposed lattice to study its interaction with Cs cations. To standardize the initial configuration, all molecules were placed equidistantly on the perovskite surface. Self-consistent iterative convergence was achieved at a threshold of 1.0×10-4 eV/atom, and atomic positions were relaxed until the maximum force on each atom was below 0.05 eV/Å.

2. Supplementary figures

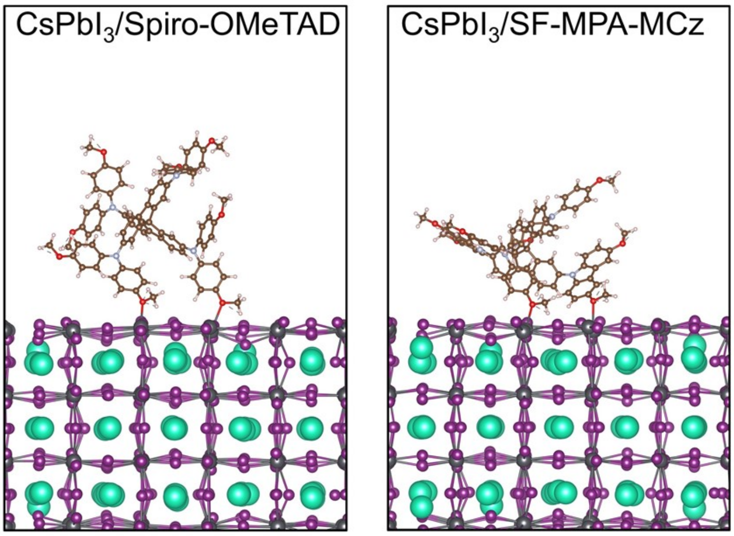

Fig. S1 DFT calculation of the interaction between Spiro-OMeTAD, SF-MPA-MCz, and the exposed perovskite surface.

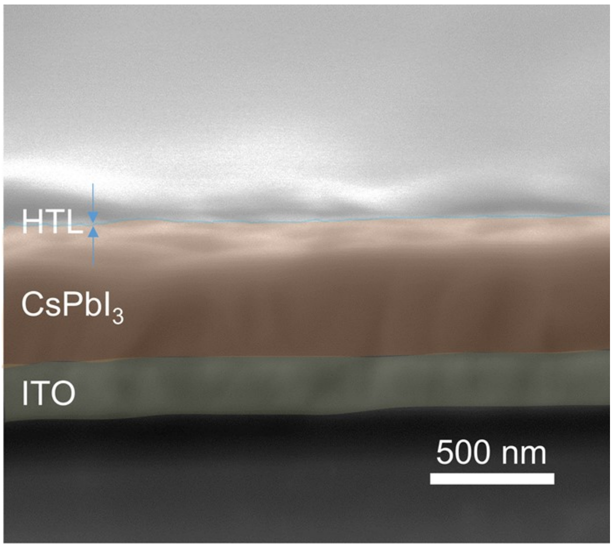

Fig. S2 Cross-sectional SEM image of sample that used in XPS.

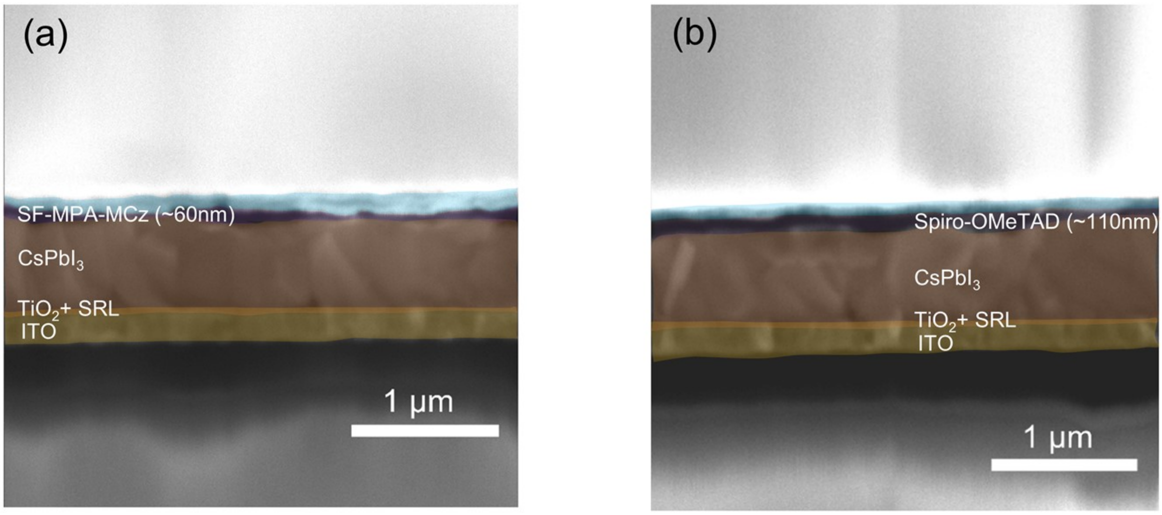

Fig. S3 Cross-sectional SEM images of (a) Spiro-OMeTAD and (b) SF-MPA-MCz based devices.

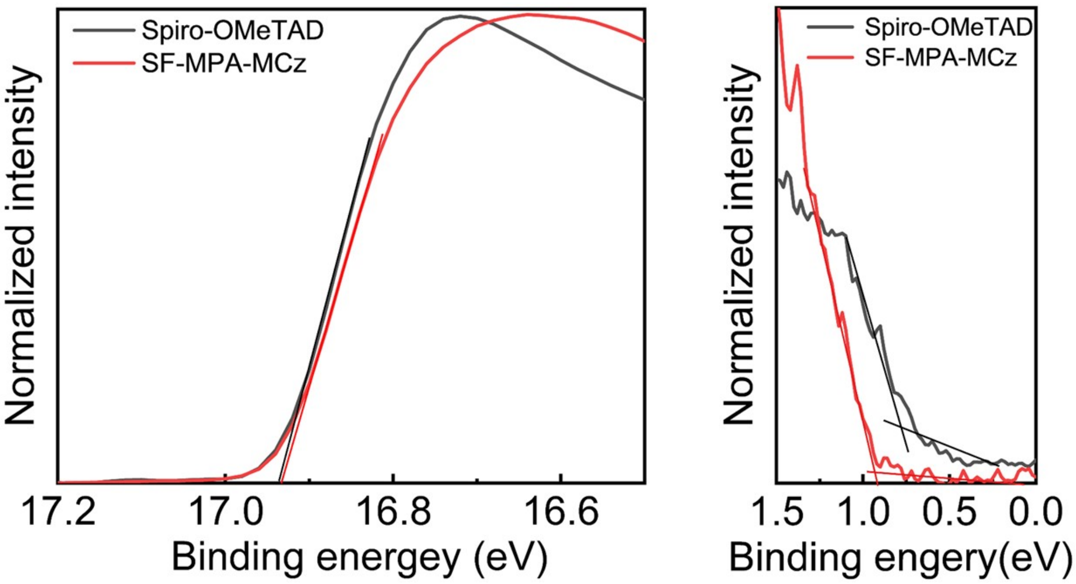

Fig. S4 UPS spectra of Spiro-OMeTAD and SF-MPA-MCz films.

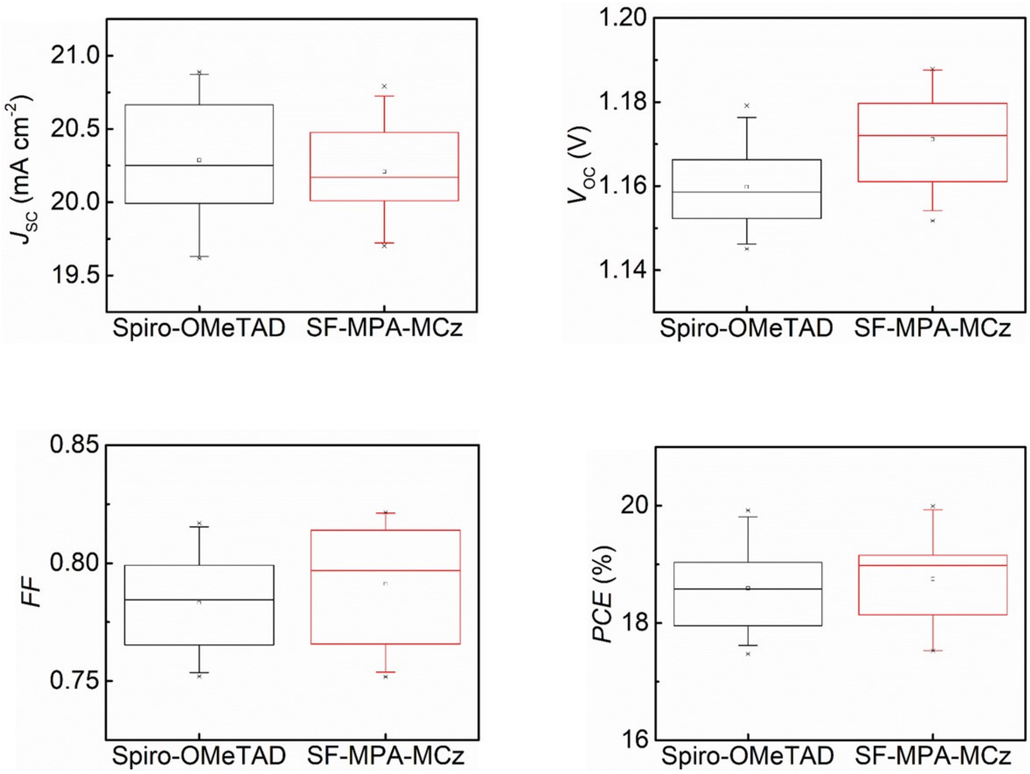

Fig. S5 J_{SC}, V_{OC}, *FF* and *PCE* distribution of the Spiro-OMeTAD and SF-MPA-MCz based PSCs (active areas of 0.16 cm^2). 20 devices were fabricated and studied in each condition.

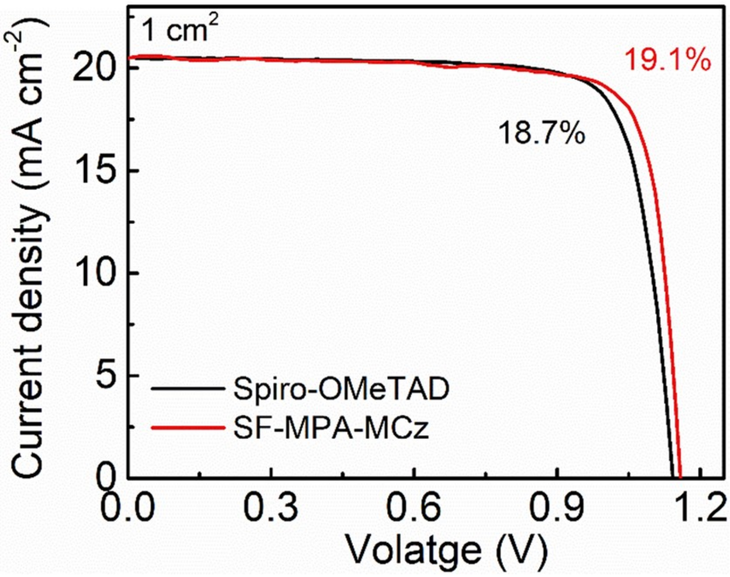

Fig. S6 *J*-*V* characteristics of 1 cm^2 PSCs based on Spiro-OMeTAD and SF-MPA-MCz, respectively.

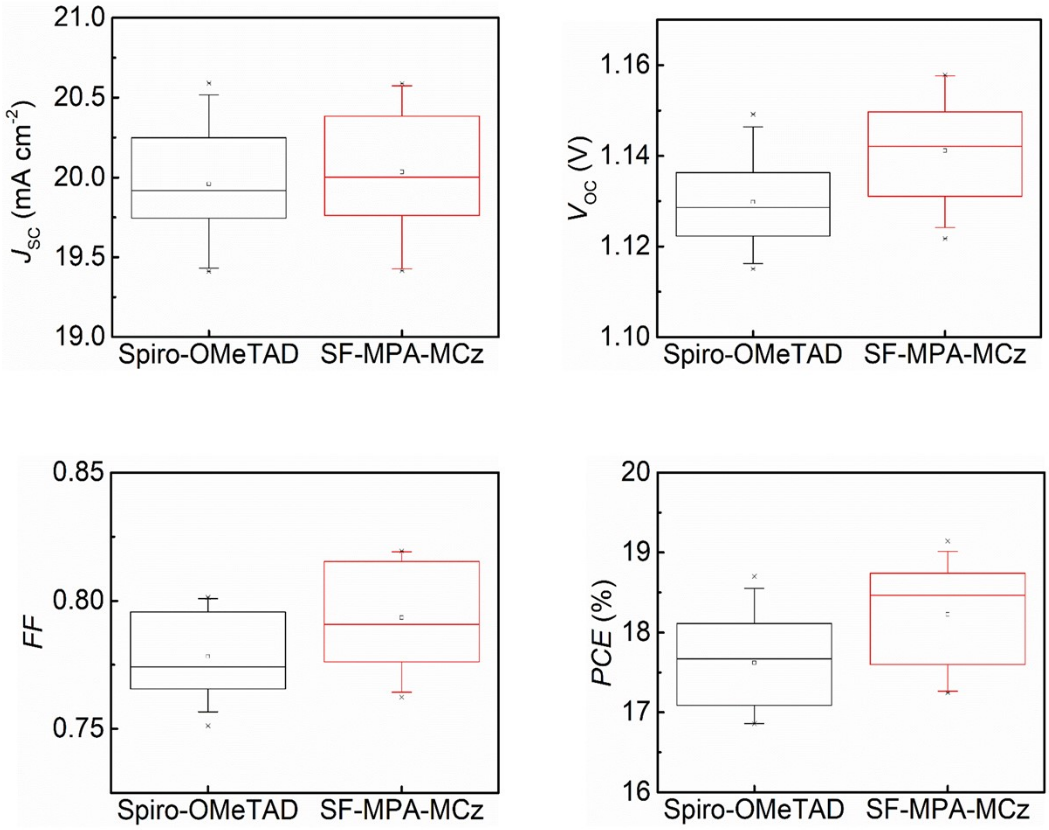

Fig. S7 J_{SC}, V_{OC}, *FF* and *PCE* distribution of the Spiro-OMeTAD and SF-MPA-MCz based PSCs (active areas of 1 cm^2). 20 devices were fabricated and studied in each condition.

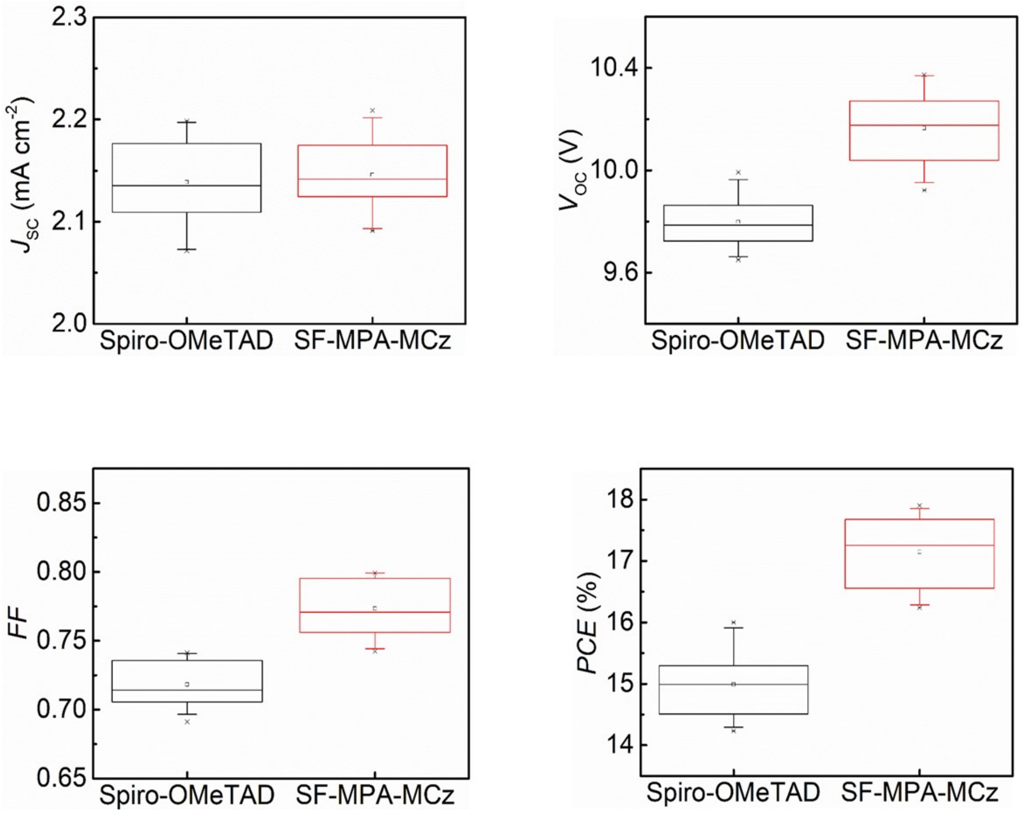

Fig. S8 J_{SC}, V_{OC}, *FF* and *PCE* distribution of the Spiro-OMeTAD and SF-MPA-MCz based PSMs (aperture areas of 27.8 cm^2). 8 devices were fabricated and studied in each condition.

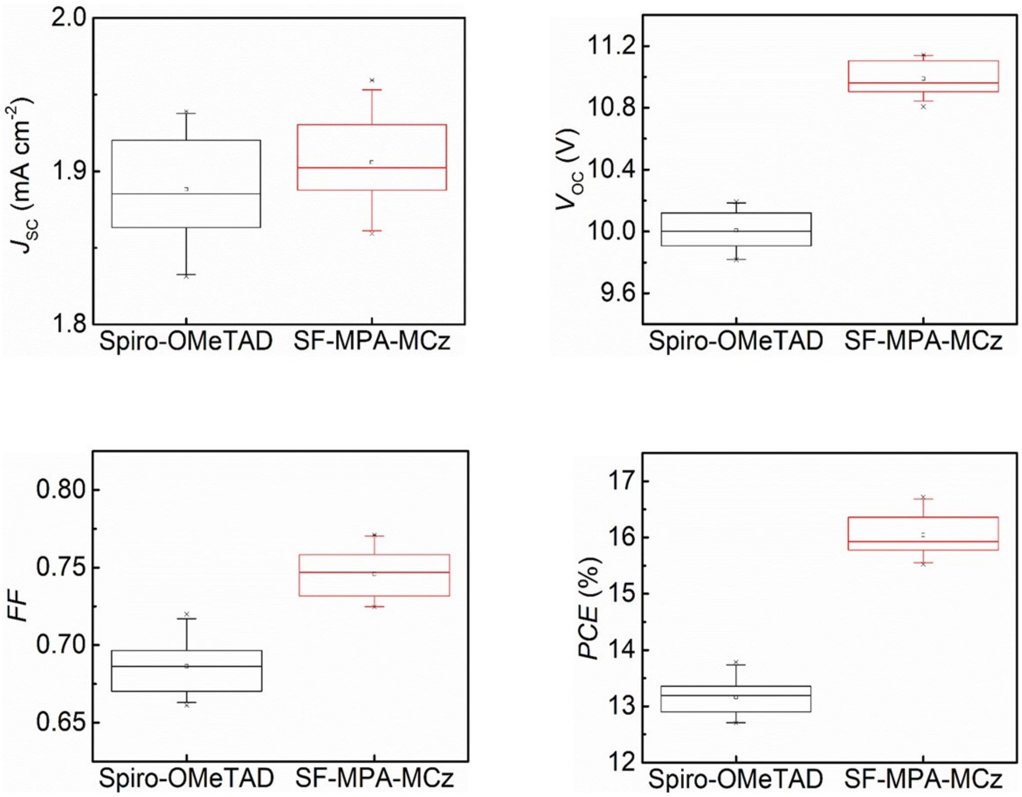

Fig. S9 J_{SC}, V_{OC}, *FF* and *PCE* distribution of the Spiro-OMeTAD and SF-MPA-MCz based PSMs (aperture areas of 186 cm^2). 8 devices were fabricated and studied in each condition.

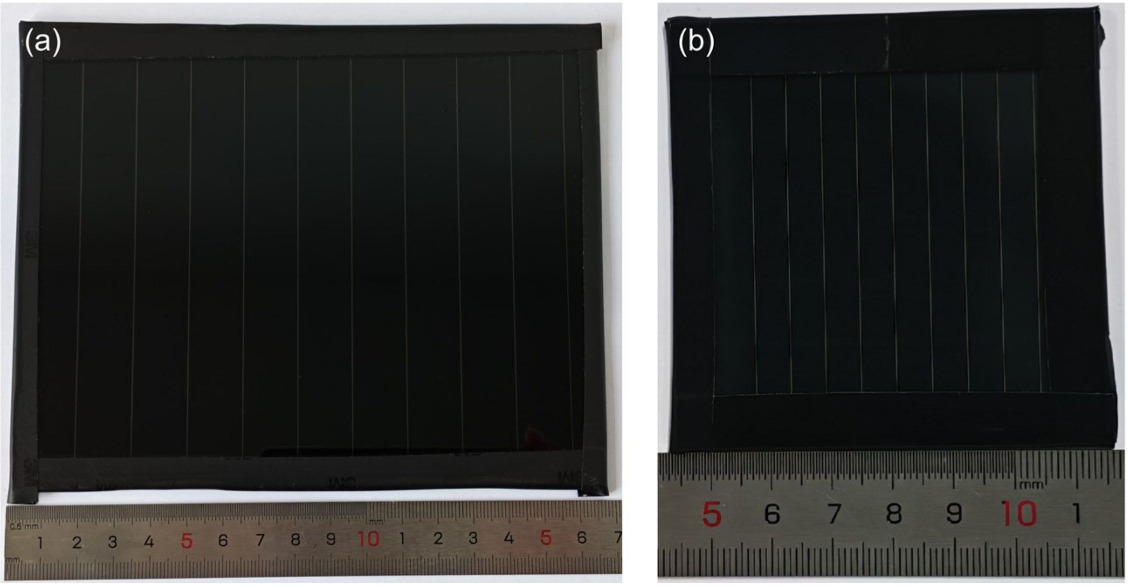

Fig. S10 Photographs of the (a) 186 cm^2 and (b) 27.8 cm^2 modules.

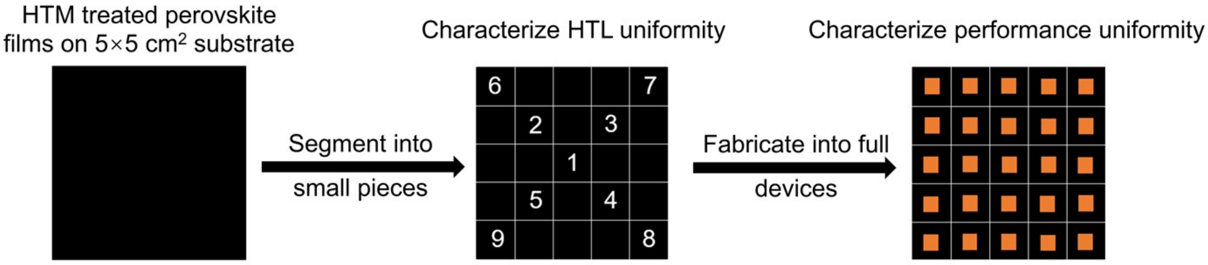

Fig. S11 Schematic diagram illustrating the uniformity characterization process for HTM-coated perovskite films and devices. Perovskite films were prepared on 5 × 5 cm^2 pre-patterned ITO/ETL/Perovskite substrates, followed by the deposition of HTMs. The films were then segmented into smaller pieces for uniformity characterization using AFM, and each segment was fabricated into full devices with active areas of 0.2 cm^2 to assess performance uniformity.

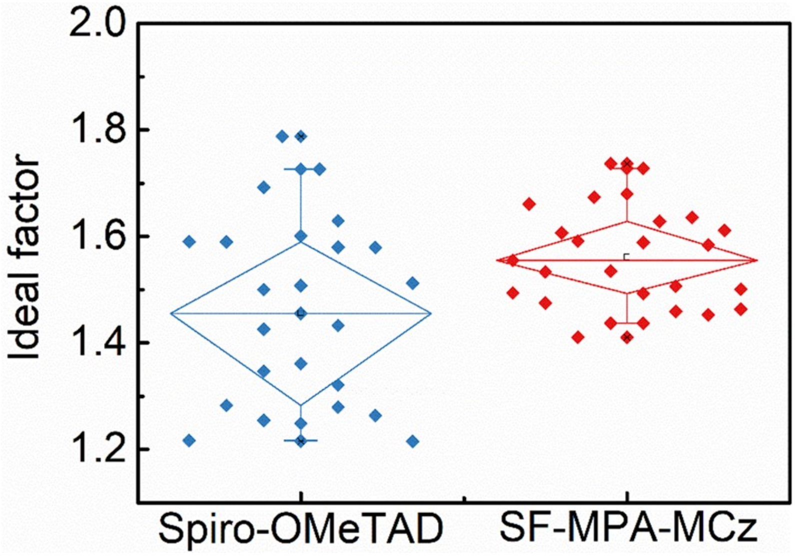

Fig. S12 Statistics of ideal factor for solar cells fabricated from small-area films segmented from Spiro-OMeTAD and SF-MPA-MCz based large-area films.

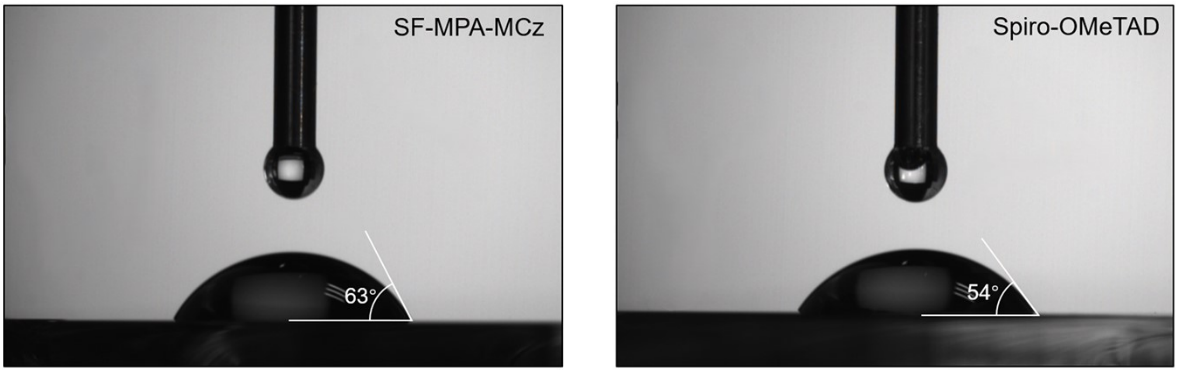

Fig. S13 Representative photographs showing the contact angles of HTMs onto perovskite.

Table S1. Summary of the champion and average photovoltaic parameters of Spiro-OMeTAD and SF-MPA-MCz based PSCs with active areas of 0.16 cm^2 under reverse voltage scan. Parameters followed by * are champion device parameters. Parameters in bracket are average parameters. Average parameters are calculated based on 20 devices in each condition.

HTM	J_{SC} (mA cm^{-2})	J_{SC} from EQE (mA cm^{-2})	V_{OC} (V)	*FF*	*PCE* (%)	*SPO* (%)
Spiro-OMeTAD	20.8* (20.3 ± 0.4)	20.0*	1.17* (1.16 ± 0.01)	0.82* (0.78 ± 0.02)	20.0* (18.6 ± 0.7)	19.4*
SF-MPA-MCz	20.7* (20.2 ± 0.3)	19.9*	1.18* (1.17 ± 0.01)	0.82* (0.79 ± 0.03)	20.0* (18.7 ± 0.7)	19.3*

Table S2. Summary of the champion and average photovoltaic parameters of Spiro-OMeTAD and SF-MPA-MCz based PSCs with active areas of 1 cm^2 under reverse voltage scan. Parameters followed by * are champion device parameters. Parameters in bracket are average parameters. Average parameters are calculated based on 20 devices in each condition.

HTM	J_{SC} (mA cm^{-2})	V_{OC} (V)	*FF*	*PCE* (%)	*SPO* (%)
Spiro-OMeTAD	20.5*	1.14*	0.80*	18.7*	18.1*
	(20.0 ± 0.3)	(1.13 ± 0.01)	(0.78 ± 0.02)	(17.6 ± 0.6)	
SF-MPA-MCz	20.5*	1.15*	0.81*	19.1*	18.5*
	(20.0 ± 0.4)	(1.14 ± 0.01)	(0.79 ± 0.02)	(18.2 ± 0.6)	

Table S3. Summary of the champion and average photovoltaic parameters of Spiro-OMeTAD and SF-MPA-MCz based PSMs (9 sub-cells, aperture areas of 27.8 cm^2) under reverse voltage scan. Parameters followed by * are champion device parameters. Parameters in bracket are average parameters. Average parameters are calculated based on 8 devices in each condition.

HTM	J_{SC} (mA cm^{-2})	V_{OC} (V)	*FF*	*PCE* (%)	*SPO* (%)
Spiro-OMeTAD	2.19*	9.9*	0.74*	16.0*	15.3*
	(2.14 ± 0.04)	(9.8 ± 0.1)	(0.72 ± 0.02)	(15.0 ± 0.5)	
SF-MPA-MCz	2.20*	10.3*	0.79*	17.9*	17.3*
	(2.15 ± 0.03)	(10.2 ± 0.1)	(0.77 ± 0.02)	(17.1 ± 0.6)	

Table S4. Summary of the champion and average photovoltaic parameters of Spiro-OMeTAD and SF-MPA-MCz based PSMs (10 sub-cells, aperture areas of 186 cm^2) under reverse voltage scan. Parameters followed by * are champion device parameters. Parameters in bracket are average parameters. Average parameters are calculated based on 8 devices in each condition.

HTM	J_{SC} (mA cm^{-2})	V_{OC} (V)	*FF*	*PCE* (%)	*SPO* (%)
Spiro-OMeTAD	1.93*	10.1*	0.71*	13.8*	13.0*
	(1.89 ± 0.03)	(10.0 ± 0.1)	(0.69 ± 0.02)	(13.2 ± 0.3)	
SF-MPA-MCz	1.95*	11.1*	0.77*	16.7*	16.0*
	(1.91 ± 0.03)	(11.0 ± 0.1)	(0.75 ± 0.02)	(16.0 ± 0.4)	

Table S5. Summary of the PCEs for the state-of-the-art inorganic-perovskite based solar modules.

No.	3D perovskite	Area(cm^2)	Type	Years	Champion PCE	Ref.
1	$CsPbI_3$	25.3	n-i-p	2024	18.6	8
2	$CsPbI_3$	23.9	n-i-p	2025	19.2	9
3	$CsPbI_3$	16	n-i-p	2025	19.8	10
4	$CsPbI_3$	64	p-i-n	2024	17.39	11
5	$CsPbI_3$	12.44	n-i-p	2025	19.32	12
6	$CsPbI_3$	12.82	n-i-p	2025	18.22	13
7	$CsPbI_3$	28.17	n-i-p	2023	16.89	14
8	$CsPbI_3$	12	n-i-p	2023	16.6	15
9	graded $CsPbI_{3-x}Br_x$	112	n-i-p	2021	13.82	16
10	$CsPbI_3$	18.08	n-i-p	2023	18.43	17
11	$CsPbI_3$	25	p-i-n	2022	14.64	18
12	$CsPbI_3$	186	n-i-p		186	This work

Table S6. TRPL fitting parameters of of perovskite films coated with different HTMs.

	τ_1 (ns)	τ_2 (ns)	τ_{avg} (ns)
perovskite/Spiro-OMeTAD	1.96	35.57	33.37
perovskite/SF-MPA-MCz	0.77	11.00	9.92

Table S7. Summary of operational stabilities of all-inorganic perovskite based devices under MPP tracking.

No.	Area (cm^2)	Champion PCE	Ageing time	Retaining PCE	Year	Ref.
1	16	19.8	950 h	80%	2025	19
2	64	17.39	1000 h	81.4%	2024	11
3	12.44	19.32	650 h	86%	2025	12
4	112	13.82	1000 h	90%	2021	16
5	25	14.64	1000 h	85%	2022	18
6	25	11.58	1000 h	91.2%	2019	20
7	16	11.8	500 h	95%	2020	10
8	19.8	10.94	200 h	80%	2022	21
9	186	16.7	4000 h	80%		This work

Reference

1 X. Wang, M. Wang, Z. Zhang, D. Wei, S. Cai, Y. Li, R. Zhang, L. Zhang, R. Zhang, C. Zhu, X. Huang, F. Gao, P. Gao, Y. Wang and W. Huang, *Research*, 2024, **7**, 0332.

2 T. Liu, X. Zhao, X. Zhong, Q. C. Burlingame, A. Kahn and Y.-L. Loo, *ACS Energy Lett.*, 2022, **7**, 3531-3538.

3 J. Xing, Q. Wang, Q. Dong, Y. Yuan, Y. Fang and J. Huang, *Phys. Chem. Chem. Phys.*, 2016, **18**, 30484-30490.

4 J. Zhao, Y. Deng, H. Wei, X. Zheng, Z. Yu, Y. Shao, J. E. Shield and J. Huang, *Sci. Adv.*, 2017, **3**, eaao5616.

5 Y. Yuan, J. Chae, Y. Shao, Q. Wang, Z. Xiao, A. Centrone and J. Huang, *Adv. Energy Mater.*, 2015, **5**, 1500615.

6 Q. Emery, M. Remec, G. Paramasivam, S. Janke, J. Dagar, C. Ulbrich, R. Schlatmann, B. Stannowski, E. Unger and M. Khenkin, *ACS Appl. Mater. Interfaces*, 2022, **14**, 5159-5167.

7 M. V. Khenkin, E. A. Katz, A. Abate, G. Bardizza, J. J. Berry, C. Brabec, F. Brunetti, V. Bulovic, Q. Burlingame, A. Di Carlo, R. Cheacharoen, Y.-B. Cheng, A. Colsmann, S. Cros, K. Domanski, M. Dusza, C. J. Fell, S. R. Forrest, Y. Galagan, D. Di Girolamo, et al., *Nat. Energy*, 2020, **5**, 35-49.

8 Y. Jiang, X. Sun, T. Liu, W. Zhang, P. Xu, B. Li, X. Zhao and W. Guo, *Angew. Chem. Int. Ed.*, 2024, **63**, e202410721.

9 X. Sun, P. Zhang, T. Liu, B. Tian, P. Xu, Y. Jiang, J. Zhang, Y. Tang, Z. Hu, W. Zhang, Z. Zhang, X. Zhao and W. Guo, *Angew. Chem. Int. Ed.*, 2025, **64**, e202501164.

10 C. Liu, Y. Yang, J. D. Fletcher, A. Liu, I. W. Gilley, C. B. Musgrave Iii, Z. Wang, H. Zhu, H. Chen, R. P. Reynolds, B. Ding, Y. Ding, X. Zhang, R. Skackauskaite, H. Wan, L. Zeng, A. S. R. Bati, N. Shibayama, V. Getautis, B. Chen, et al., *Nat. Energy*, 2025, **10**, 981-990.

11 J. H. Heo, J. K. Park, H. J. Lee, E. H. Shin, S. Y. Hong, K.-H. Hong, F. Zhang and S. H. Im, *Adv. Mater.*, 2024, **36**, e2408387.

12 H. Wang, B. Li, F. Liu, W. Zhan, M. Feng, J. Guo, S. Wang, Y. Liang, Y. Fan, Y. Chen, Y. Miao and Y. Zhao, *Adv. Funct. Mater.*, 2025, **35**, 2423397.

13 X. Liu, J. Zhang, H. Wang, Y. Miao, T. Guo, L. K. Ono, S. Yuan, Y. Wang, P. Ji, H. Chen, C. Zhang, T. Li, C. Ding, S. Mariotti, X. Huo, I.-N. Rabehi, H. Wang, Y. Zhao and Y. Qi, *Joule*, 2024, **8**, 2851-2862.

14 C. Liu, X. Sun, Y. Yang, O. A. Syzgantseva, M. A. Syzgantseva, B. Ding, N. Shibayama, H. Kanda, F. F. Tirani, R. Scopelliti, S. Zhang, K. G. Brooks, S. Dai, G. Cui, M. D. Irwin, Z. Shao, Y. Ding, Z. Fei, P. J. Dyson and M. K. Nazeeruddin, *Sci. Adv.*, 2023, **9**, eadg0087.

15 S. Tan, C. Tan, Y. Cui, B. Yu, Y. Li, H. Wu, J. Shi, Y. Luo, D. Li and Q. Meng, *Adv. Mater.*, 2023, **35**, e2301879.

16 J. H. Heo, F. Zhang, C. Xiao, S. J. Heo, J. K. Park, J. J. Berry, K. Zhu and S. H. Im, *Joule*, 2021, **5**, 481-494.

17 S. S. Mali, J. V. Patil, J.-Y. Shao, Y.-W. Zhong, S. R. Rondiya, N. Y. Dzade and C. K. Hong, *Nat. Energy*, 2023, **8**, 989-1001.

18 J. H. Heo, F. Zhang, J. K. Park, H. J. Lee, D. S. Lee, S. J. Heo, J. M. Luther, J. J. Berry, K. Zhu and S. H. Im, *Joule*, 2022, **6**, 1672-1688.

19 R. Chen, Y. Hui, B. Wu, Y. Wang, X. Huang, Z. Xu, P. Ruan, W. Zhang, F. Cheng, W. Zhang, J. Yin, J. Li and N. Zheng, *J. Mater. Chem. A*, 2020, **8**, 9597-9606.

20 J. H. Heo, D. H. Kim, J. K. Park, Y. K. Choi, D. S. Lee and S. H. Im, *ACS Appl. Mater. Interfaces*, 2019, **11**, 43066-43074.

21 S. S. Mali, J. V. Patil, S. R. Rondiya, N. Y. Dzade, J. A. Steele, M. K. Nazeeruddin, P. S. Patil and C. K. Hong, *Adv. Mater.*, 2022, **34**, e2203204.